JOURNAL OF MATERIALS SCIENCE **38** (2003) 291 – 305

An investigation of the micromechanisms of fatigue crack growth in structural gas turbine engine alloys

C. MERCER
Department of Mechanical and Aerospace Engineering, and the Princeton Materials Institute, Princeton University, Princeton, NJ 08544, USA

S. SHADEMAN
Department of Materials Science and Engineering, The Ohio State University, Columbus, OH 43210, USA

W. O. SOBOYEJO
Department of Mechanical and Aerospace Engineering, and the Princeton Materials Institute, Princeton University, Princeton, NJ 08544, USA
E-mail: Soboyejo@princeton.edu

This paper presents an overview of fatigue fracture modes in selected structural alloys employed in gas turbine engines. These include the mechanisms of fatigue crack growth in the near-threshold, Paris and high-ΔK regimes obtained from Ti-6Al-4V, Inconel 718 and PWA 1472 (a single crystal nickel-based superalloy of similar chemical composition to Inconel 718). Fatigue fracture modes in these materials are shown to be strong functions of the stress intensity factor range, ΔK, and the maximum stress intensity factor, K_{max}. Fatigue mechanism maps are also presented to show the parametric ranges of ΔK and K_{max} corresponding to the different fatigue fracture modes. © *2003 Kluwer Academic Publishers*

1. Introduction

Fatigue is thought to account for 80–90% of all engineering failures [1]. Nevertheless, there are only a few limited tools for the diagnoses of fatigue failures [2–4]. In most cases, these tools are in the form of fracture atlases that show representative fractographic images that are associated with fracture under cyclic loading [2]. However, fatigue fracture modes are highly dependent on the applied stress intensity factor range, ΔK, and the maximum stress intensity factor, K_{max} [4–10]. There is, therefore, a need for detailed studies of the effects of ΔK and K_{max} on the 10]. There is, therefore, a need for detailed studies of the effects of ΔK and K_{max} on the micromechanisms of fatigue crack growth in structural alloys, particularly the alloys used in gas turbine engine applications.

Two of the most important classes of materials used in gas turbine engines are titanium alloys and nickel-based superalloys. Titanium alloys are employed extensively in the fan and compressor (low to intermediate temperature) sections of gas turbine engines, due to their low density, good specific properties and weldability [11–14]. Nickel-based superalloys, on the other hand, are primarily used in the hot sections of the engine, chiefly for combustor and turbine components [13–17]. The types of nickel-based superalloys used range from forged, polycrystalline materials for turbine disc applications [13, 14], to single crystal alloys used in turbine blades [7, 13, 14, 17]. Diagnosis of fatigue in such materials requires detailed failure analysis in order to provide fractographic evidence of the effect of crack driving forces on fracture modes [18, 19].

This paper presents an overview of fatigue fracture modes in structural gas turbine engine alloys. Following a brief description of the alloy microstructures and experimental procedures, the fatigue fracture modes are presented as functions of ΔK and K_{max}. Fatigue mechanism maps are also presented for selected alloys to illustrate a compact approach to the presentation of fatigue fracture mode information. Finally, the implications of the results are discussed for the analyses/diagnoses of fatigue failures.

2. Material

In an effort to identify some general trends, a range of gas turbine engine materials were examined in this study. These include: polycrystalline Inconel 718, PWA 1472 (a single crystal material based on Inconel 718) and Ti-6Al-4V.

2.1. Polycrystalline Inconel 718

The Inconel 718 material was obtained in the form of a 5.5 mm thick plate from Wyman Gordon, Houston, TX. The plate was cut from a triple melted (vacuum induction melting + vacuum arc remelting + electroslag remelting) billet supplied by Specialty Metals, Inc.,

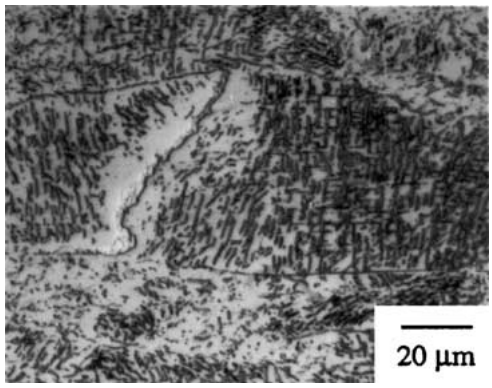

Figure 1 Optical micrograph showing general microstructure of forged, polycrystalline IN 718 alloy.

New Hartford, NY. The microstructure of the polycrystalline IN718 is shown in Fig. 1. This consists of nickel-rich face-centered cubic (f.c.c.) solid solution nickel (γ phase) with an average equiaxed grain size of $\sim$30 μm. A moderate density of lenticular Ni_3Nb precipitates are present within the γ matrix (Fig. 1).

2.2. Single crystal PWA 1472

The single crystal Inconel 718 variant (PWA 1472) was supplied by Pratt and Whitney, West Palm Beach, FL, in the form of cast cylindrical bars with a diameter of $\sim$15 mm. The [111] direction was parallel to the longitudinal axis of the bars. The microstructure of this single crystal alloy, however, is dendritic in nature (Fig. 2). It consists of dendrites of Ni-rich f.c.c. phase and very coarse (40 μm–130 μm) interdendritic Ni_3 Nb precipitates. The low magnification micrograph shown in Fig. 2a, clearly shows the dendritic morphology of the single crystal microstructure.

2.3. Ti-6Al-4V

The Ti-6Al-4V forging that was used in this study was supplied by Wyman Gordon, Houston, TX. It was mill annealed to produce a near-equiaxed microstructure (Fig. 3) with a β volume fraction of $\sim$22.7% and an average equiaxed α grain size of $\sim$19.6 μm. In an effort to examine the effects of heat treatment, sections

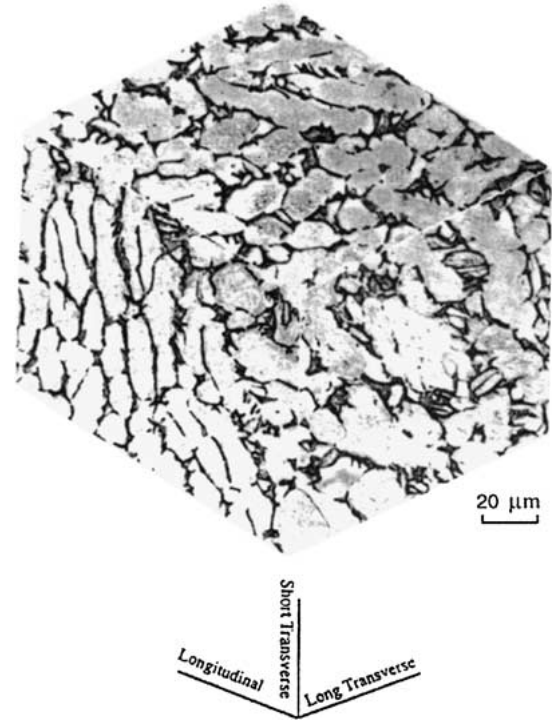

Figure 3 Triplanar optical micrograph of the mill-annealed TI-6Al-4V alloy (microstructure D).

of the Ti-6Al-4V alloy were heat-treated at 1070°C for 30 minutes (above the β transus) prior to cooling at different rates (25°C/min, 3°C/min and 1°C/min) to 400°C. They were then argon-quenched to room temperature. The resulting colony microstructures are shown in Fig. 4. The associated microstructural unit sizes (obtained via quantitative image analyses) are summarized in Table I, in which the basic mechanical properties are also provided. As expected from prior work on α/β titanium alloys [20, 21], the microstructure becomes coarser with decreasing cooling rate. Furthermore, the fracture toughness increases with increasing colony size. However, there is no clear effect of microstructure on strength and ductility (Table I).

3. Experimental procedures

The fatigue experiments were carried out on single-edge-notched bend (SENB) specimens with lengths

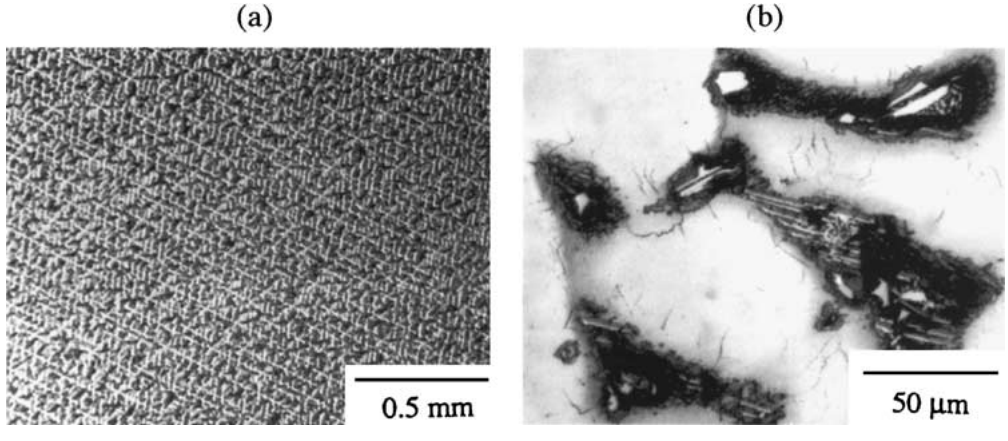

Figure 2 Optical micrographs showing general microstructure of PWA 1472.

TABLE I Summary of microstructural parameters and basic mechanical properties

Micro-structure	β layer continuity (Yes/no)	Widmanstatten colony size (μm)	α lath size (μm)	Volume (%, α)	Volume (%, β)	UTS MPa	ε_f (%)	Fracture toughness, (K_{Ic}, MPa$\sqrt{m}$)
A	no	118.20 ± 2.74	3.45 ± 0.61	66.65	33.35	912	7	121
B	no	168.88 ± 5.03	6.59 ± 0.21	78.56	21.44	878	11.9	109[a]
C	yes	312.50 ± 17.22	14.14 ± 0.88	77.91	22.09	934	7.6	152[a]
D	yes	19.57 ± 2.22[b]		77.26	22.74	922	15	57[a]

[a]Not valid according to ASTM 399-90.
[b]α grain size (μm).
Microstructure A: 1070°C/30 min./cool@25°C/min. to 400°C/Ar quench to RT Microstructure B: 1070°C/30 min./ cool@3°C/min. to 400°C/Ar quench to RT Microstructure C: 1070°C/30 min./cool@1°C/min. to 400°C/Ar quench to RT Microstructure D: Mill Annealed (as received)

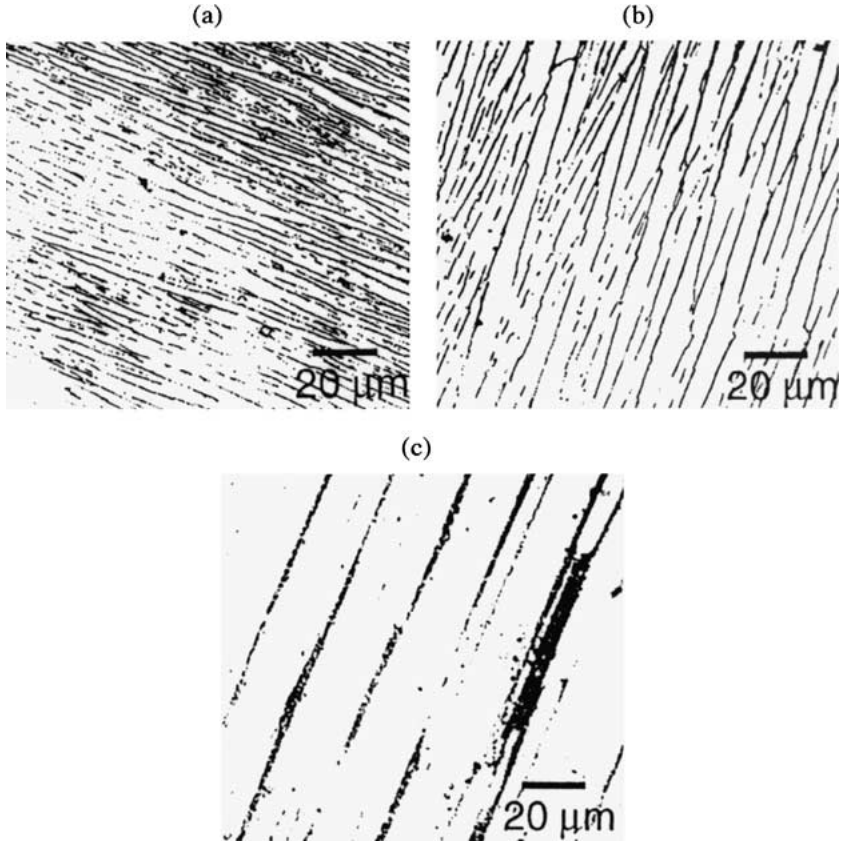

Figure 4 Optical micrographs of the Widmanstatten TI-6Al-4V alloys; (a) microstructure A, (b) microstructure B, and (c) microstructure C.

of ~60 mm. The SENB specimens had either square (~6 mm × 6 mm) or rectangular (~3 or 6 mm × 12 mm) cross-sections. The initial notch-length-to-width rations (a/W) were ~0.25. In the case of the PWA 1472 single crystal material, the SENB specimens were machined from the bars such that the longitudinal axis of the specimen corresponded to the ⟨111⟩ crystallographic direction in the material and the crack growth direction corresponded to the ⟨110⟩ crystallographic direction. Fatigue crack growth testing was then carried out under computer controlled, Mode I (three point bend) loading conditions using a cyclic frequency of 10 Hz. The fatigue tests were carried out at stress ratios, $R = K_{min}/K_{max}$, between 0.1 and 0.8. Tests were carried out under either (i) contant load amplitude or (ii) decreasing/increasing ΔK conditions.

In the decreasing/increasing ΔK tests, the specimens were pre-cracked at moderately high ΔK levels, prior to load-shedding at a fixed rate, $C = -0.08$ mm^{-1}. This was continued until crack growth rates of ~10^{-8} mm/cycle (approximately one lattice spacing) were reached. This was taken to correspond to the fatigue threshold stress intensity factor range, ΔK_{th}. Subsequently, a load increasing scheme ($C = +0.08$) was applied to grow the cracks out to failure from an intermediate stress-intensity factor range. Due to the initial mismatch in the fatigue crack growth rates (associated with initial overload effects and crack front mismatch), the measured data was only used after the load-increasing fatigue crack growth rate data merged with the load-decreasing data.

Crack extension was monitored with a either, direct current potential drop (d.c.p.d.) system, a notch-mouth clip gauge compliance system, or a Questar QM1 telescope with a resolution of 2.5 μm (Questar is a trademark of the Questar Corporation, New Hope, PA). Specimens were cycled until catastrophic failure occurred. The fatigue fracture surfaces were then

examined under a scanning electron microscope (SEM) to determine the variation in fracture modes with ΔK and K_{max}. The distance from the notch mouth to the transition points between fracture modes was measured in the SEM. This distance is equal to the crack length at which a transition to a different fracture mode occurred. The ΔK and K_{max} values that correspond to this crack length could then be determined from the fatigue crack growth rate data. Hence, the variation in fatigue fracture mode with ΔK and K_{max} could be evaluated.

4. Results

4.1. Fatigue crack growth rates

4.1.1. (a) Nickel-base superalloys

The da/dN versus ΔK fatigue crack growth (FCG) curves obtained for both nickel-based alloys at each of the four stress ratios employed are presented in Figs 5 and 6. The near-threshold, Paris and high ΔK regimes of each curve are discernible in all cases, but are more apparent in the case of the polycrystalline material. It is evident from the plots presented in Fig. 6 that the single crystal alloy exhibits noticeably higher fatigue thresholds and lower near-threshold fatigue crack growth rates than the polycrystalline alloy. Stable fatigue crack growth was observed at K_{max} levels below 50 MPa$\sqrt{}$m in both alloys. The data is in good agreement with the results obtained from other studies of similar alloys [17, 22–31].

The Paris exponents, m, for each alloy and stress ratio are presented in Table I. The values of m in Table I for the polycrystalline alloy are typical of those one would expect for a conventional metallic material. Such materials generally have Paris exponents of between 2 and 4 [4]. However, the Paris exponents of the single crystal alloy are noticeably higher (at 4.6–8.0), than those of the more conventional, polycrystalline material.

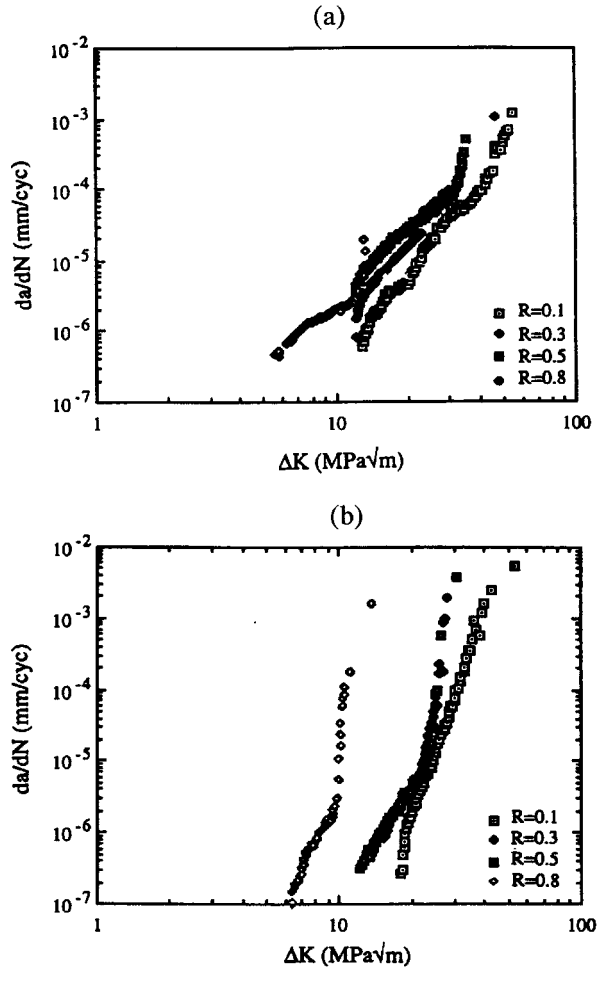

Figure 5 Fatigue crack growth curves (da/dN versus ΔK) for (a) polycrystalline IN 718 and (b) PWA 1472, at stress ratios of 0.1, 0.3, 0.5 and 0.8.

4.1.2. Ti-6Al-4V

The fatigue crack growth rate data obtained for Ti-6Al-4V are presented for the three colony microstructures (microstructures A-C) and the equiaxed α/β structure (microstructure D) in Figs 7 and 8. The fatigue crack growth rates increase with increasing stress ratio in each of the microstructural conditions. Furthermore, for each of the stress ratios, the microstructures A and B exhibit similar growth rates, while microstructure C (the coarsest microstructure) exhibits the slowest crack growth rates, especially at higher ΔK levels (Fig. 7). The difference in the fatigue crack growth rate data are attributed largely to the role of roughness-induced crack closure. This has been examined in detail in a separate paper [32].

4.2. Fractography

4.2.1. Polycrystalline Inconel 718

Typical fatigue fracture surfaces corresponding to the near-threshold regime and lower portion of the Paris regime of both alloys when tested at a stress ratios between 0.1–0.5 are presented in Fig. 9a and b, respectively. The mode of fracture under cyclic loading in both regimes appeared to be a transgranular, crystallographic mode, as can be seen by the sharp, angular facets in the fracture surfaces (Fig. 9a and b). Very fine fatigue striations were observed on some of the crystallographic facets, indicating the presence of very localized plasticity during fatigue crack growth in the near-threshold and lower Paris regimes.

The transition to a classical striation type of fracture mode [33, 34] corresponding to greater levels of plasticity was observed at stress intensity factor ranges that correspond to the upper Paris regime (Fig. 9c). This is generally indicative of a pure fatigue crack growth mechanism that is controlled by duplex slip processes that give rise to crack-tip blunting [4]. It is interesting to note that the transition from the crystallographic fracture mode to the striation mechanism occurred when the crack-tip opening displacement was approximately equal to the size of the facets on the crystallographic fracture surface, (approximately 5 μm). At high ΔK levels a ductile-dimpled fracture mode was observed in addition to the fatigue striations as the K_{max} levels approached the fracture toughness of the IN 718 material (Fig. 9d).

Hence, the departure of the Paris line in the high ΔK regime is thought to be due to the additional contributions from static or monotonic (ductile dimpled)

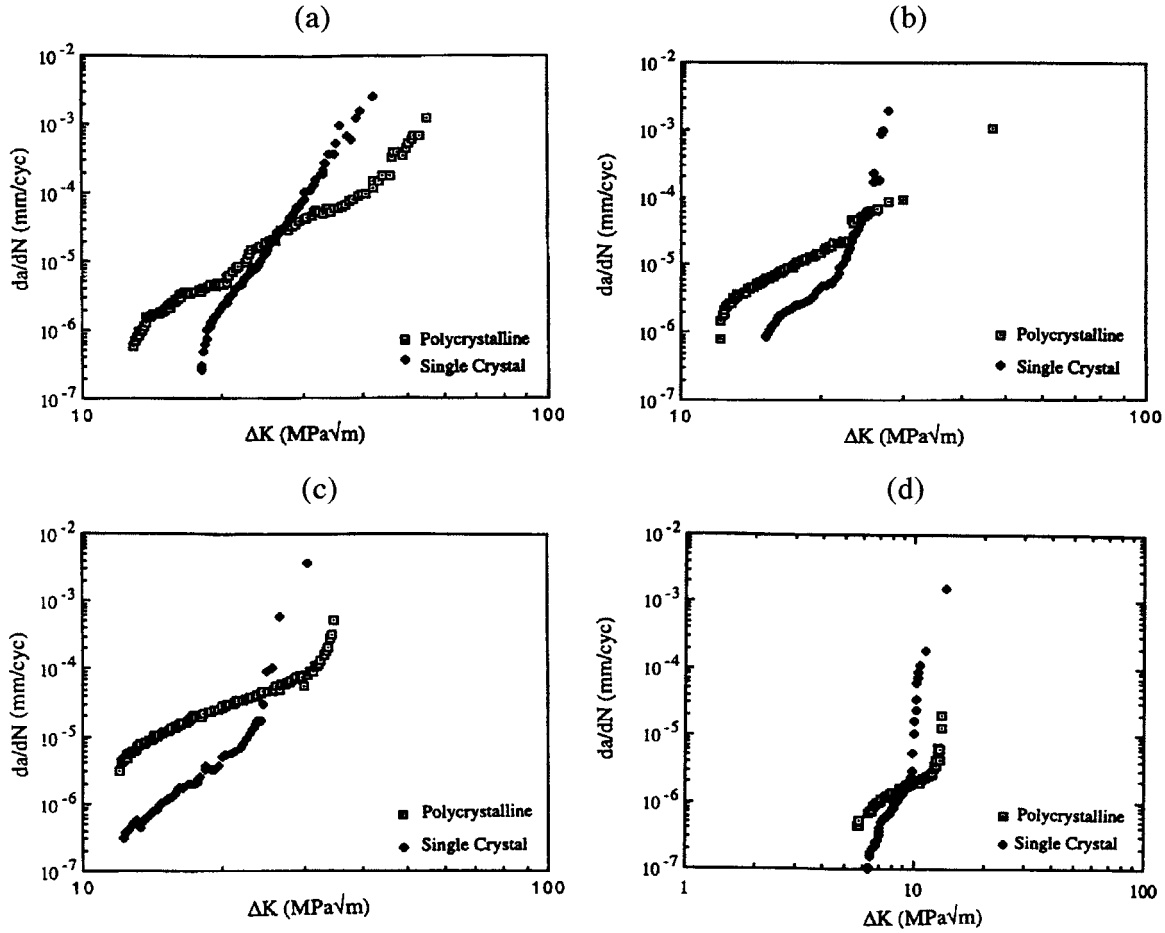

Figure 6 Comparison of fatigue crack growth curves for polycrystalline IN 718 and PWA 1472, at stress ratios of (a) 0.1, (b) 0.3, (c) 0.5 and (d) 0.8.

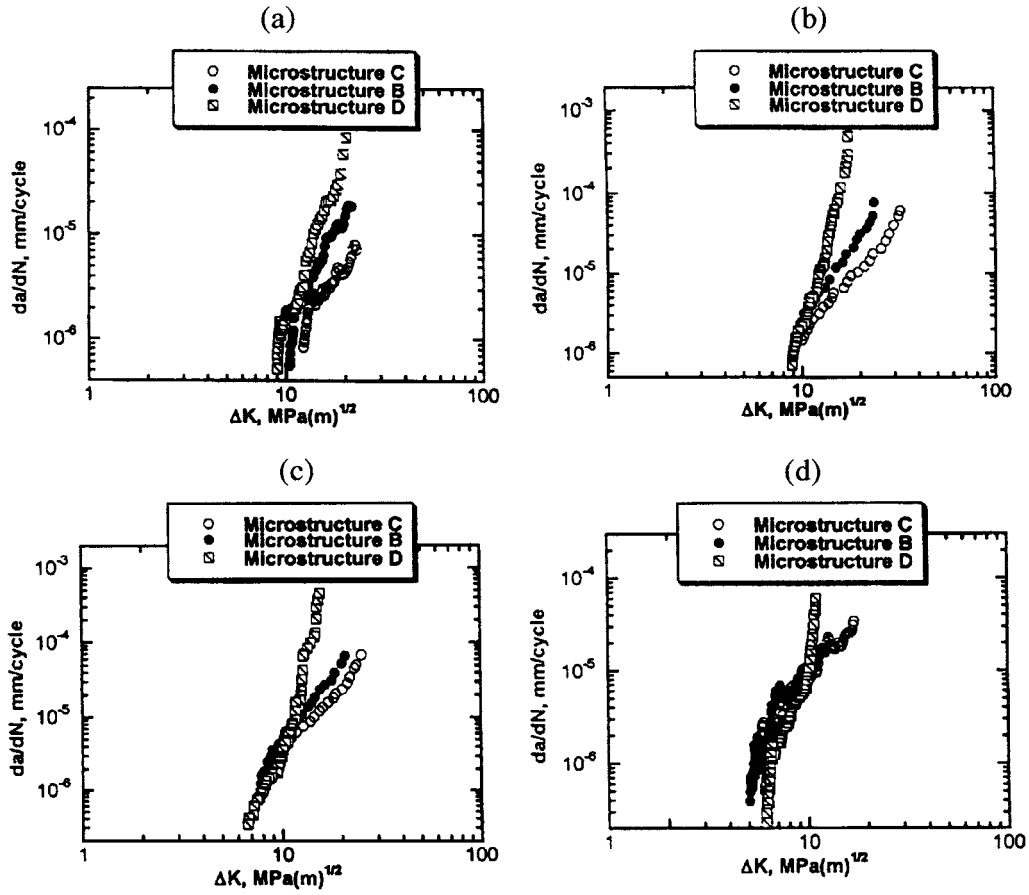

Figure 7 Effects of microstructural coarsening on fatigue crack growth rates at stress ratios of (a) 0.1, (b) 0.3, (c) 0.5 and (d) 0.8.

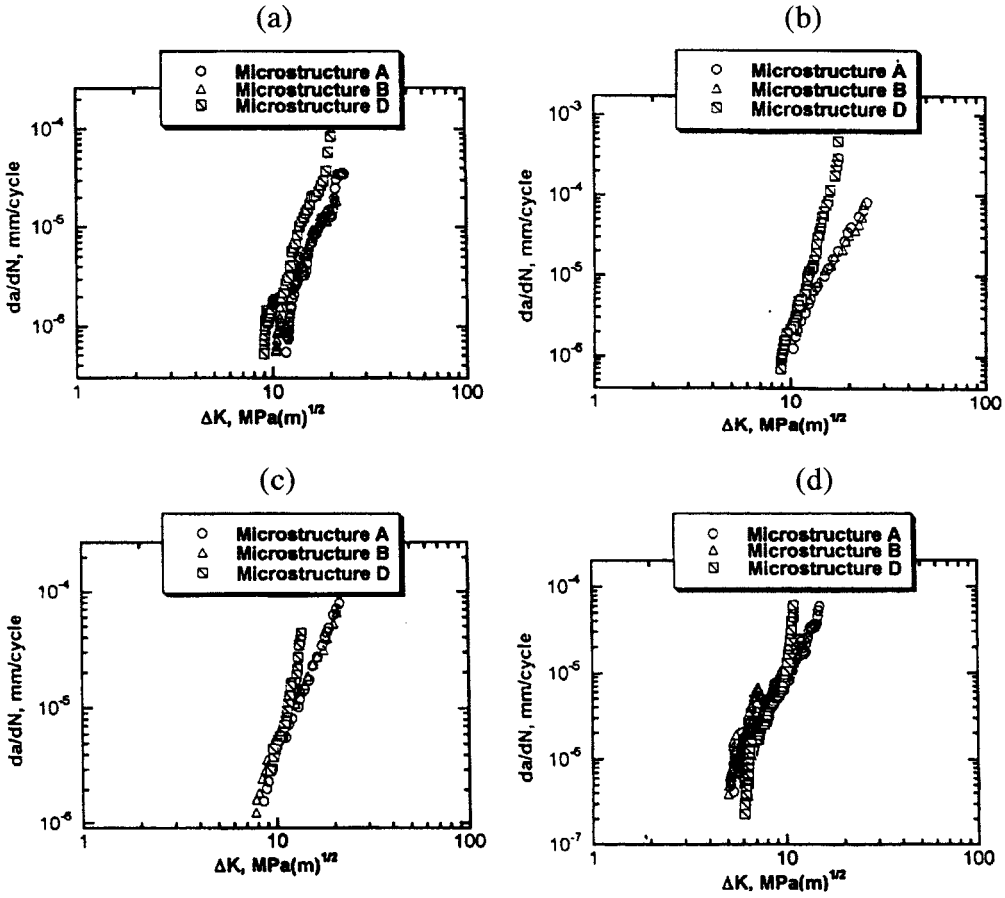

Figure 8 Effects of beta volume fraction on fatigue crack growth rates at stress ratios of (a) 0.1, (b) 0.25, (c) 0.5 and (d) 0.8.

fracture modes (Fig. 9d). The tensile overload region of the fracture surface is also compared with the fracture modes in the different fatigue regimes in Fig. 9. The classical ductile-dimpled fracture mechansim observed is similar to the monotonic fracture mode observed in the high ΔK fatigue regime.

At a stress ratio of 0.8, components of the crystallographic fracture mode were present throughout the Paris regime and well into the high ΔK regime (Fig. 10). Very fine striations were observed on the crystallographic facets in the Paris regime (Fig. 10b). Secondary cracking was also apparent on the fracture surfaces within the Paris regime. In the high ΔK regime at $R = 0.8$, the ductile-dimpled static fracture mode was observed to be active as in the case for $R = 0.1$. However, as already mentioned, the crystallographic fracture mode was also present in this regime (Fig. 10c).

4.2.2. Single crystal PWA 1472

The fracture modes observed in the cast, single crystal alloy were very different from those observed in the polycrystalline material. The fracture modes in the single crystal alloy also appeared to be less dependent on stress ratio. In fact, the fracture mechanisms observed in each regime of the fatigue crack growth curve were essentially the same at all stress ratios employed. Only the relative proportions of each mechanism observed on the entire fracture surface appeared to very with stress ratio.

A typical SEM micrograph of the fracture surface corresponding to the near-threshold regime in this single crystal material, is shown in Fig. 11a. The fracture mechanism observed in this regime is also crystallographic, as was the case for the polycrystalline material (Fig. 9a). However, although the mode of fracture appears to be similar to the polycrystalline IN 718, the nature of the fracture surface shown in Fig. 11a is very different. The fracture surface exhibits much greater relief with the crystallographic facets being considerably more pronounced, as can be clearly seen in Fig. 11a. Also, the fine striations on the crystallographic facets are much more prominent than those observed on the facets in the polycrystalline alloy. This may indicate a greater extent of localized plasticity in the near-threshold regime of this material, thereby giving rise to more clearly defined striations.

Fig. 11b shows the typical fracture surface corresponding to the Paris and high ΔK regimes at a stress ratio of 0.1. The mode of fracture active in both of these regimes is quite unlike anything observed in the polycrystalline material. As shown in Fig. 11b, the fracture surface resembles a cleavage fracture surface, but exhibiting a considerably coarser river pattern. Within this river pattern, narrow wavy facets or planes can be clearly seen. Fine striations are clearly visible on these facets, (Fig. 11b). This cleavage-like fracture mode appears to be the steady-state mechanism of fracture during stable fatigue crack propogation in this single crystal material. Accelerated crack growth in the high ΔK regime also appears to occur via this mechanism.

However, an abrupt change in fracture mode was observed in the upper part of the high ΔK fatigue regime, immediately prior to specimen failure. This mode

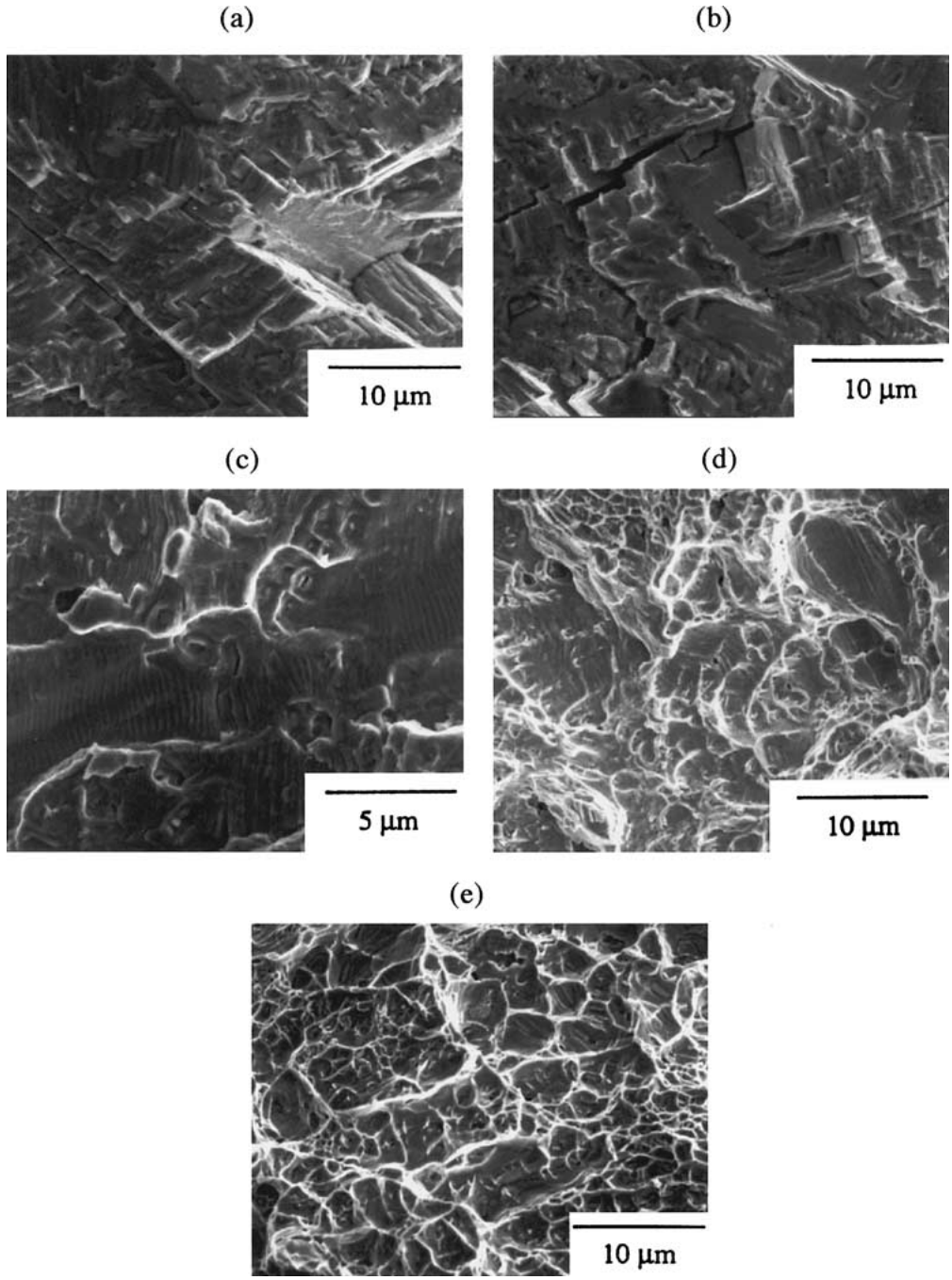

Figure 9 Scanning electron micrographs showing fracture surfaces of polycrystalline IN 718 corresponding to (a) the near-threshold regime, (b) the lower Paris regime, (c) the upper Paris regime and (d) the high ΔK regime of the fatigue crack growth curve, and (e) the tensile overload region of the specimen, for a stress ratio of 0.1.

of fracture was predominantly of the ductile-dimpled static-type, (Fig. 11c). However, the dimples were very coarse (up to 250 μm in diameter). In addition, fine fatigue striations were observed on the concave surfaces of the dimples, as shown in Fig. 11c). The mixed mode of fracture observed just piror to specimen failure is similar to that observed in the polycrystalline material but the nature of the fracture surface is different. The polycrystalline alloy shows dimples superimposed on a surface containing striations. The single crystal alloy shows a surface dominated by coarse dimples with striations present within the dimples. Fig. 11d shows the abrupt change from the cleavage-like river pattern/striation mechanism (active in the Paris and high ΔK regimes) to the ductile-dimpled/striation mechanism associated with very rapid crack growth immediately prior to specimen failure.

As stated above, the relative proportions of each mechanism was different for different stress ratios. In effect, extent of the river pattern/striation mechanism associated with steady-state fatigue crack growth in the Paris regime, and accelerated crack growth throughout most of the high ΔK regime of this alloy, became more and more suppressed as stress ratio was increased. The low magnification images presented in Fig. 12 show the reduction in the relative amount of the cleavage-like fracture mechanism observed on the fracture surface, with increasing stress ratio. At a stress ratio of 0.8 the cleavage-like fracture mode had become almost non-existent, and the material essentially exhibited

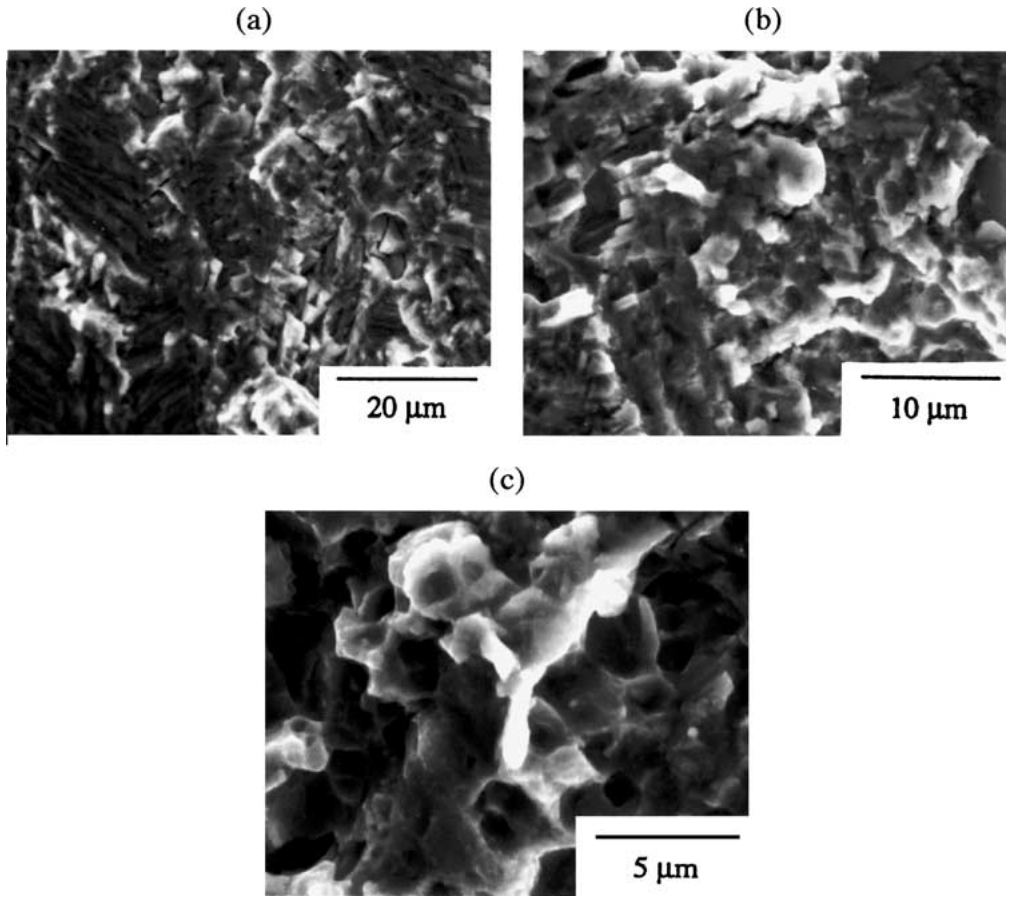

Figure 10 Scanning electron micrographs showing fracture surfaces of polycrystalline IN 718 corresponding to (a) the near-threshold regime, (b) the Paris regime and (c) the high ΔK regime of the fatigue crack growth curve, for a stress ratio of 0.8.

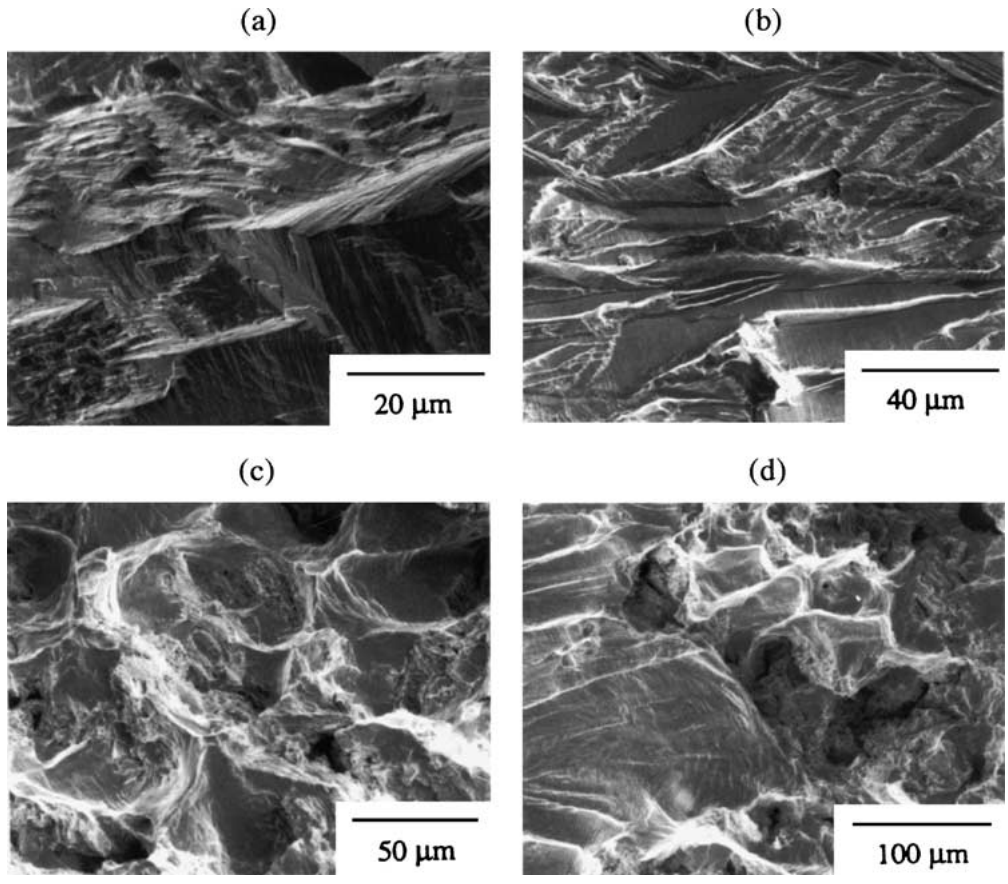

Figure 11 Scanning electron micrographs showing fracture surfaces of PWA 1472 corresponding to (a) the near-threshold regime and (b) the Paris and high ΔK regimes of the fatigue crack growth curve, and (c and d)) immediately prior to failure, for a stress ratio of 0.1.

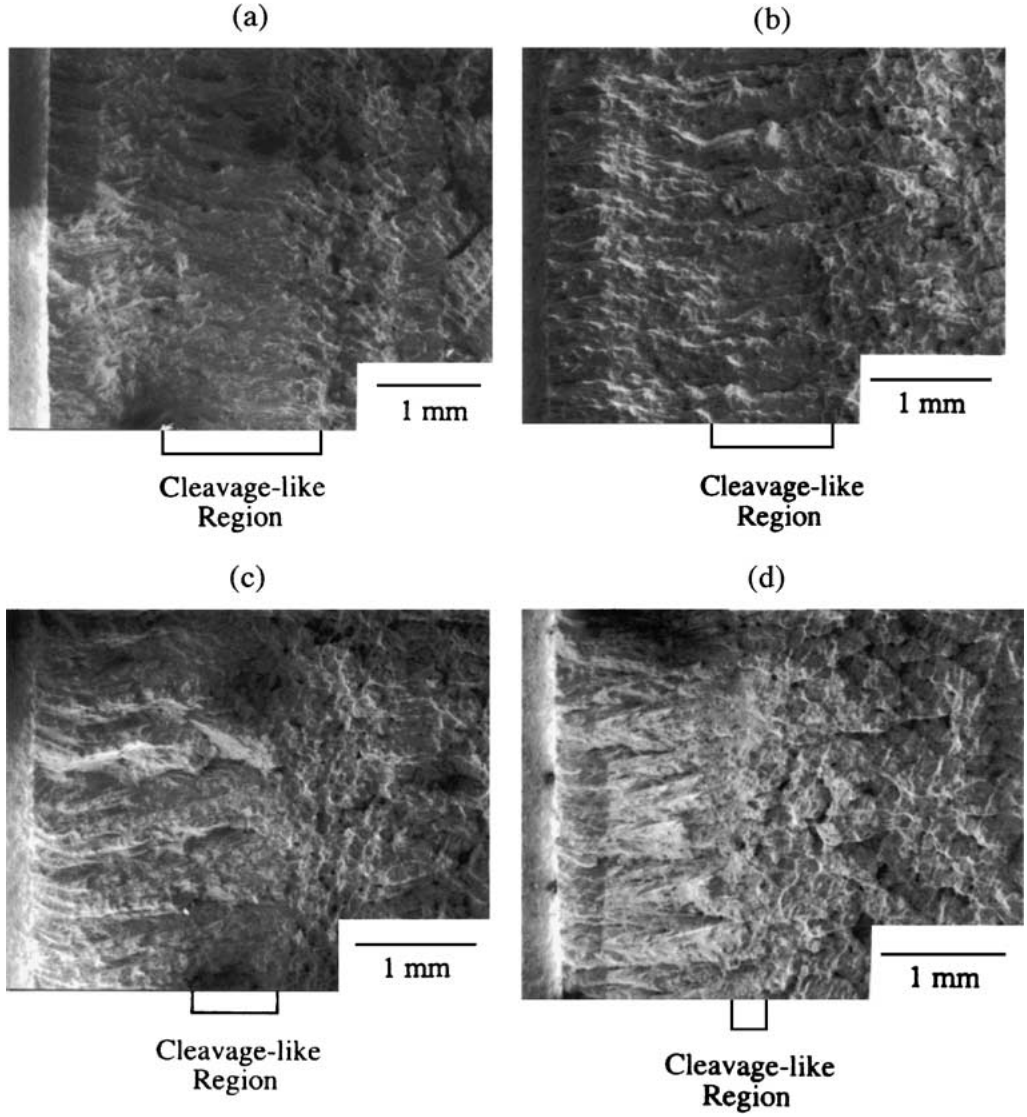

Figure 12 Low magnification scanning electron micrographs showing the reduction in relative amount of the cleavage-like fatigue fracture mechanism with increasing stress ratio in PWA 1472, for stress ratio of (a) 0.1, (b) 0.3, (c) 0.5 and (d) 0.8.

crystallographic fracture right up until the onset of catastrophic failure.

A typical fracture surface corresponding to the tensile overload region in the single crystal material is shown in Fig. 13. Evidence of dendrites can be clearly seen on the fracture surface of the tensile overload region, suggesting that fast fracture in this material is interdendritic in nature. The highly dendritic microstructure of this alloy (Fig. 2), therefore, appears to promote fracture between dendrites in this alloy during tensile overload. The interdendritic nature of the fast fracture regions of the single crystal specimens can also be seen in the low magnification images presented in Fig. 12.

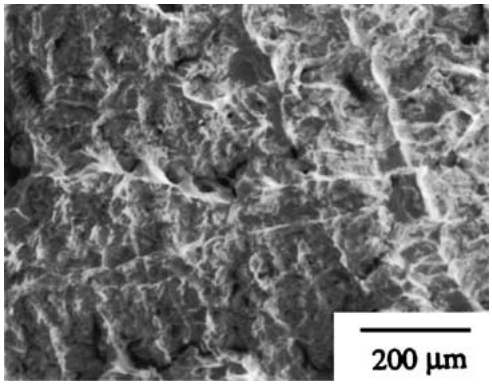

Figure 13 Scanning electron micrograph showing evidence of dendrites in the tensile overload region of PWA 1472.

4.2.3. Ti-6Al-4V

The fatigue fracture observed in the Ti-6Al-4V alloy at a stress ratio of 0.1, are presented in Figs 14–17 for microstructures A–D, respectively. In the case of the lamellar microstructures (A–C), the fracture modes were very similar at similar ΔK levels. In the near-threshold regimes, flat, cleavage-like fracture modes were observed (Figs. 14a, 15a and 16a). Evidence of fracture surface debris was also present on the fracture surfaces of the specimens tested at a stress ratio of 0.1 (Figs 14a, 15a and 16a).

In contrast, a step-like, crystallographic fracture mode was observed in the mid-ΔK regime in microstructures A–C (Figs 14b, 15b and 16b). These persisted into the high ΔK regime, where a higher incidence of secondary cracking was also observed (Figs 14c, 15c and 16c). Furthermore, no evidence of

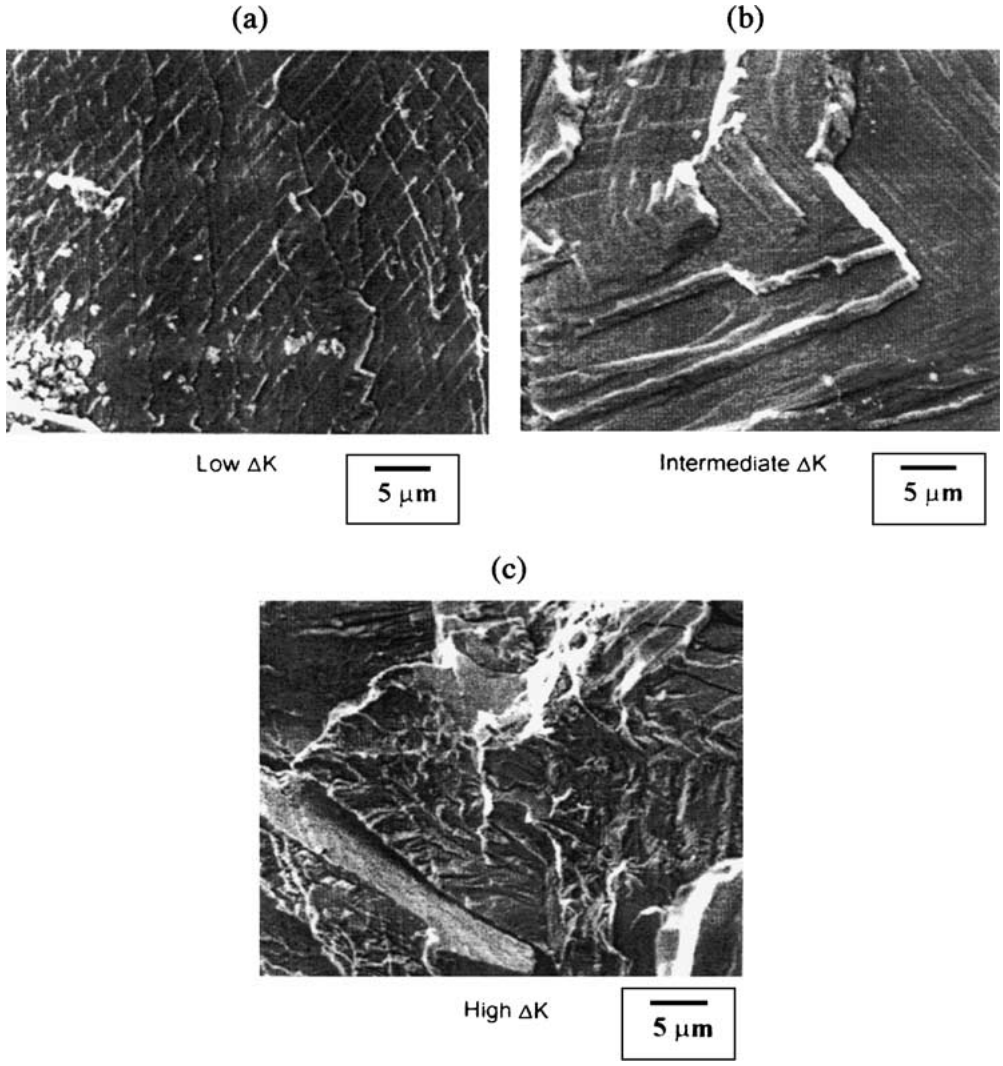

Figure 14 Scanning electron micrographs showing fracture surfaces of Ti-6Al-4V (microstructure A) in; (a) near-threshold regime, (b) mid-ΔK regime, and (C) high ΔK regime.

fracture surface debris was observed above the near-threshold regime.

In the case of the equiaxed α/β structure (microstructure D), a flat, cleavage-like fracture mode was observed in the near-threshold regime at a stress ratio of 0.25 (Fig. 17a). A transition to fatigue striations was observed in the mid-ΔK regime (Fig. 17b), while crack growth in the high ΔK regime occurred by a combination of striations and ductile-dimples (Fig. 17c). The incidence of ductile-dimples also increased with increasing ΔK in the high ΔK regime.

5. Discussion

5.1. Nickel-base superalloys

Fatigue crack growth studies has shown the single crystal alloy based on IN 718 to have a higher fatigue threshold than the conventional polycrystalline IN 718. However, as noted previously, once fatigue crack growth does occur, the slopes of the steady-state portions of the fatigue crack growth curves (Paris exponents) are considerably higher in the case of the single crystal material. As can be seen from the plots in Fig. 6, the curves for the two alloys intersect or cross-over for all four stress ratios employed. This means that below the point of intersection, fatigue crack growth rates will be faster in the polycrystalline material. However, above the cross-over point, the single crystal material will exhibit faster crack growth rates.

The higher fatigue thresholds and slower fatigue crack growth rates at lower ΔK levels in the single crystal material are thought to be due to the fact that in single crystal materials fatigue crack growth is highly dependent on crystallography at low ΔK levels. Cracks will grow along preferred crystallographic planes (in this case {111} planes) until the crack driving force becomes high enough to allow crack growth in the Mode I (crack-opening) direction. However, once crack growth in the Mode I direction begins, the absence of grain boundaries acting as barriers to fatigue crack propagation, will cause crack growth rates to increase more rapidly than in similar polycrystalline materials. This explains the observed faster crack growth rates in the single crystal material at higher ΔK levels.

The major differences in fracture mechanisms were observed to be those associated with steady-state fatigue crack growth in the Paris regime. The cross-over points between the fatigue crack growth curves occur in the middle of this regime. Steady-state crack growth in the polycrystalline alloy occurs by crystallographic

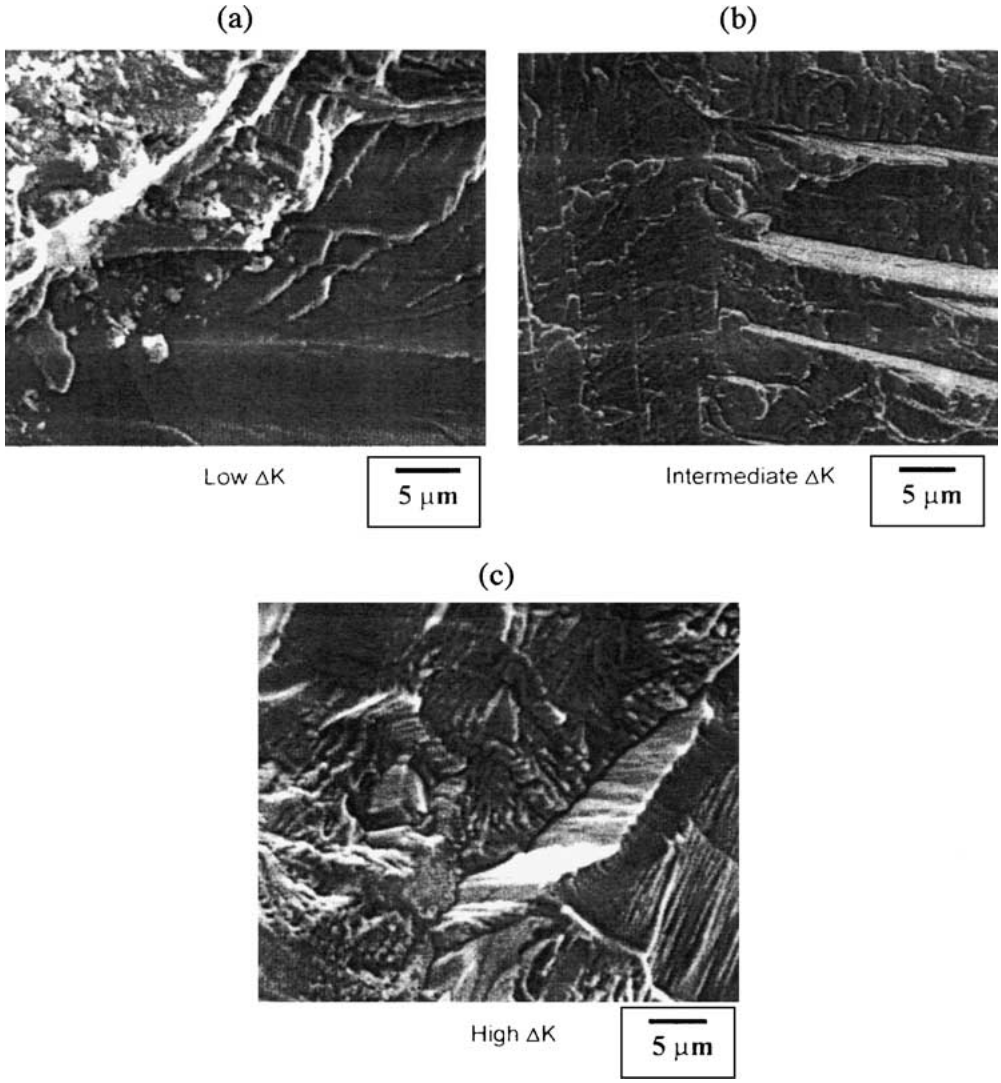

Figure 15 Scanning electron micrographs showing fracture surfaces of Ti-6Al-4V (microstructure B) in; (a) near-threshold regime, (b) mid-ΔK regime, and (C) high ΔK regime.

fracture up to approximately the middle of the Paris regime, but then, with the exception of the case when $R = 0.8$, undergoes a change to a classical plastic-blunting mechanism, as first proposed by Laird and Smith [34], which leads to the formation of relatively coarse striations.

However, the mode of fracture active throughout the entire Paris regime (and most of the high ΔK regime) for the single crystal material, at stress ratios of 0.5 and below, was very different. As described above, this fracture mechanism resembles a very coarse, cleavage fracture surface, with a river pattern consisting of wavy surfaces or planes. Very fine striations are present on these surfaces, as shown in Fig. 11b. This mechanism of cyclic fracture is not fully understood at present, although the fracture surface suggests that it may involve a combination of cleavage along preferred crystallographic planes and limited plastic-blunting giving rise to fine striations on the cleaved surfaces.

At a stress ratio of 0.8, however, neither the plastic-blunting or the river pattern fatigue mechanisms were observed. Instead, both alloys exhibited crystallographic fracture throughout the near-threshold, Paris and high ΔK regimes. The polycrystalline material also showed ductile-dimpled fracture in addition to crystallographic fracture at the onset of accelerated crack growth in the high ΔK regime. The single crystal alloy, however, exhibited an abrupt change from crystallographic fracture to ductile-dimpled fracture just prior to specimen failure. Differences in the mechanisms of crack-tip deformation in the two alloys may also be responsible for the dissimilar Paris exponents. Detailed transmission electron microscopy studies would be required to verify this postulation.

A possible reason for the faster fatigue crack growth rates at higher ΔK levels in the single crystal alloy is simply the absence of grain boundaries in the single crystal material. Grain boundaries can act as barriers to advancing crack-tips and hence may cause deflection of cracks away from the preferred direction of growth, leading to a more tortuous crack path. At higher ΔK levels, this may result is a slower overall rate of crack propagation as compared to a straight, rapidly advancing, unimpeded crack. At lower ΔK levels, cracks tend to follow preferred crystallographic directions and hence exhibit more tortuous crack paths anyway. Therefore, the absence of grain boundaries in a single crystal may give rise to less tortuous crack paths and hence increased fatigue crack growth rates at higher ΔK levels.

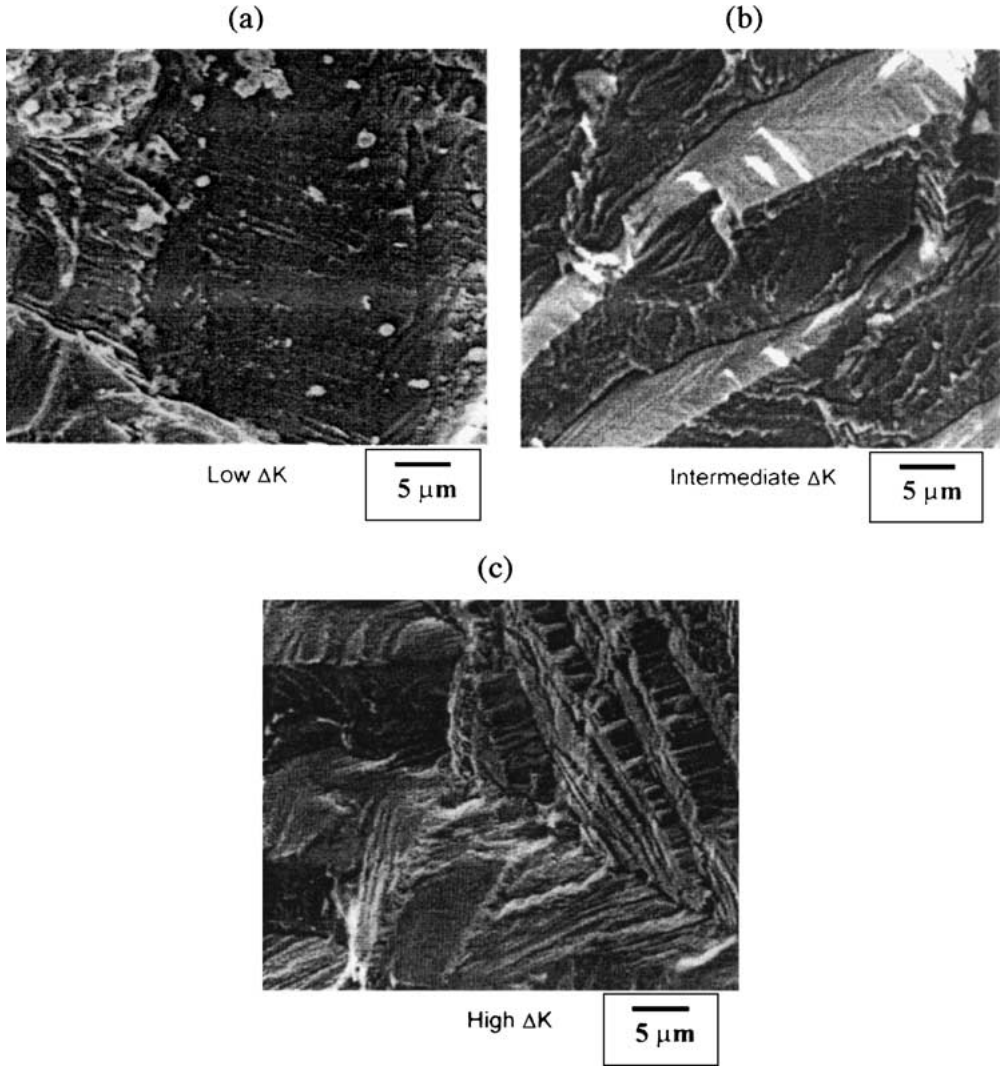

Figure 16 Scanning electron micrographs showing fracture surfaces of Ti-6Al-4V (microstructure C) in; (a) near-threshold regime, (b) mid-ΔK regime, and (C) high ΔK regime.

Another very important observation of this investigation is that the fracture mechanisms that occur during fatigue crack growth in both of these materials, are not only controlled by the stress intensity factor range (ΔK), but also by the maximum stress intensity (K_{max}). This is evident from the marked variation of fatigue crack growth rates and corresponding fracture mechanisms with stress ratio. It is generally accepted from the Paris equation that ΔK is the driving force for fatigue crack growth. However, the effects of K_{max} or R must also be assessed, since this parameter clearly affects the micromechanisms of fatigue crack growth and hence the overall fatigue behavior of these types of materials.

Fracture mechanism maps showing the active fracture mechanisms that occur under cyclic loading in these materials are presented in Fig. 18, as a plot of K_{max} and ΔK. Diagonal lines that correspond to constant stress ratio conditions radiate from the origin of the map. The map also shows a series of arcs (hyperbolae) which correspond to a transition from one fracture mode to another. These arcs intersect at a common point located on the K_{max} axis. This point corresponds to the fracture toughness of the material under monotonic loading (i.e., $\Delta K = 0$). The numerical values of these points are 75 MPa$\sqrt{}$m and 66 MPa$\sqrt{}$m for the single crystal and polycrystalline material, respectively. The fracture mode will be fully ductile-dimpled fracture under these conditions. It is clearly apparent that the transitions between each fracture mode defined by the arcs in Fig. 18 depend upon both ΔK and K_{max}.

5.2. Ti-6Al-4V

A summary of the ΔK and K_{max} levels corresponding to the different fracture modes is presented on fracture mechanism maps as shown in Fig. 19 for the different microstructures (A–D). As in the earlier fracture maps (Fig. 18), these show that the loci of the transitions in mechanisms are hyperbolae that radiate from the point of the ordinate where $K_{max} = K_{Ic}$. Also, the features on the fracture maps obtained for the colony microstructures are very similar (Fig. 19a–c). Most of these maps are dominated by the cleavage and faceted regions. In contrast, the mechanism map obtained for the mill annealed/equiaxed microstructure exhibits regimes of striations and striations + dimples, as shown in Fig. 19d. Also, it is important to note that the dashed lines in Fig. 19 correspond to the parametric

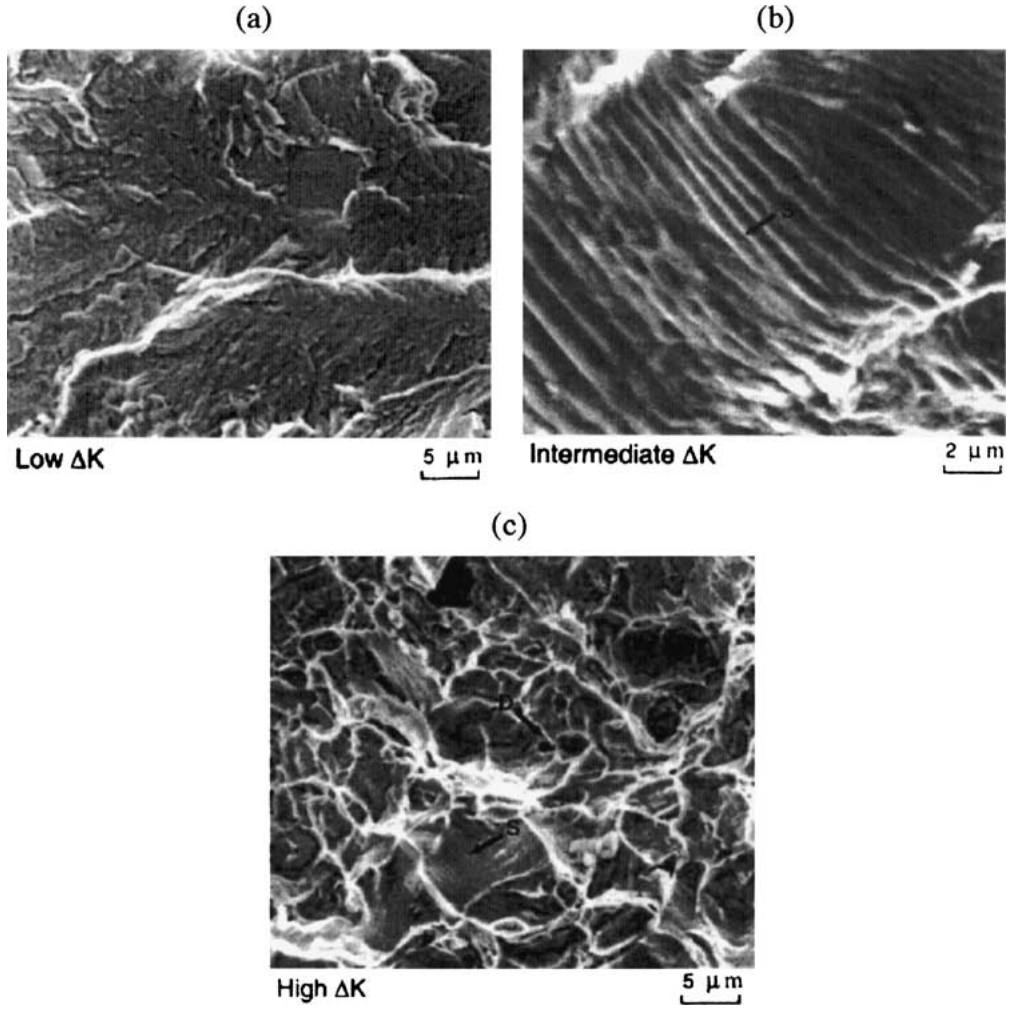

Figure 17 Scanning electron micrographs showing fracture surfaces of Ti-6Al-4V (microstructure D) in; (a) near-threshold regime, (b) mid-ΔK regime, and (C) high ΔK regime.

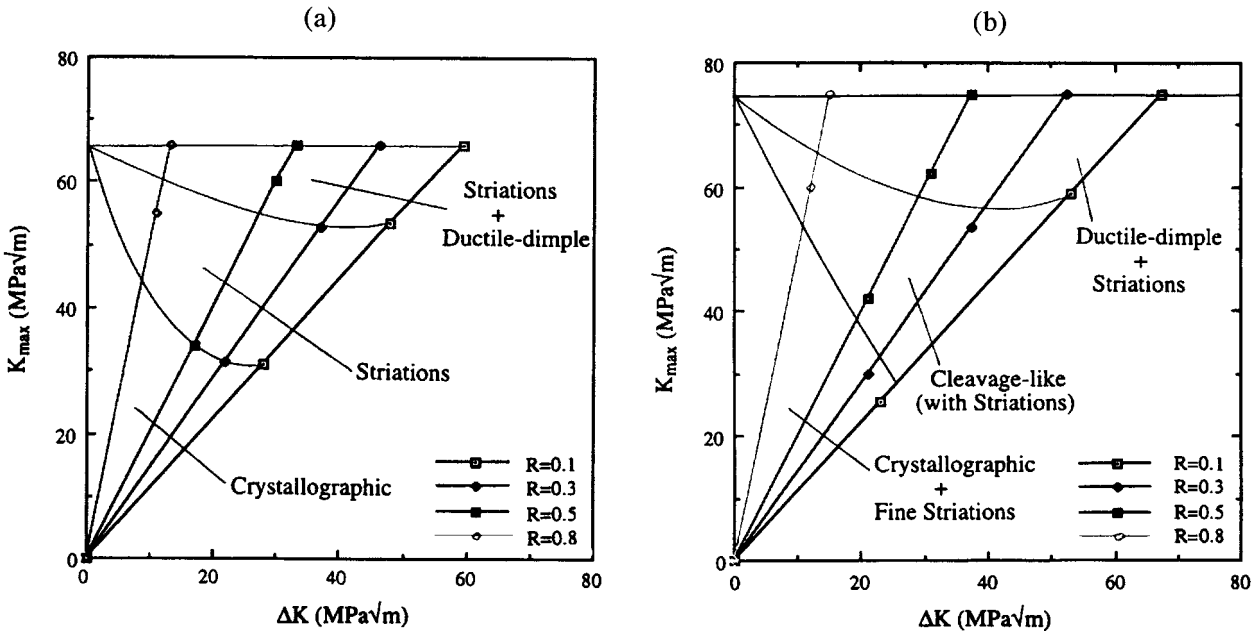

Figure 18 Fracture mechanism map showing the transitions between fatigue fracture modes as a function of ΔK and K_{max}, for (a) polycrystalline IN 718 and (b) PWA 1472.

ranges in ΔK and K_{max} over which mechanism transitions were observed to occur.

Before discussing the fracture modes in more detail, it is of interest to compare the crack growth rates in the different microstructures. For comparable β volume fractions, i.e., microstructures B, C and D with β volume fractions close to 0.2 (Table I), the fatigue crack growth rates are compared in Fig. 7. This shows clearly that the fatigue crack growth rates in microstructures B, C and D are comparable in the near-threshold regime.

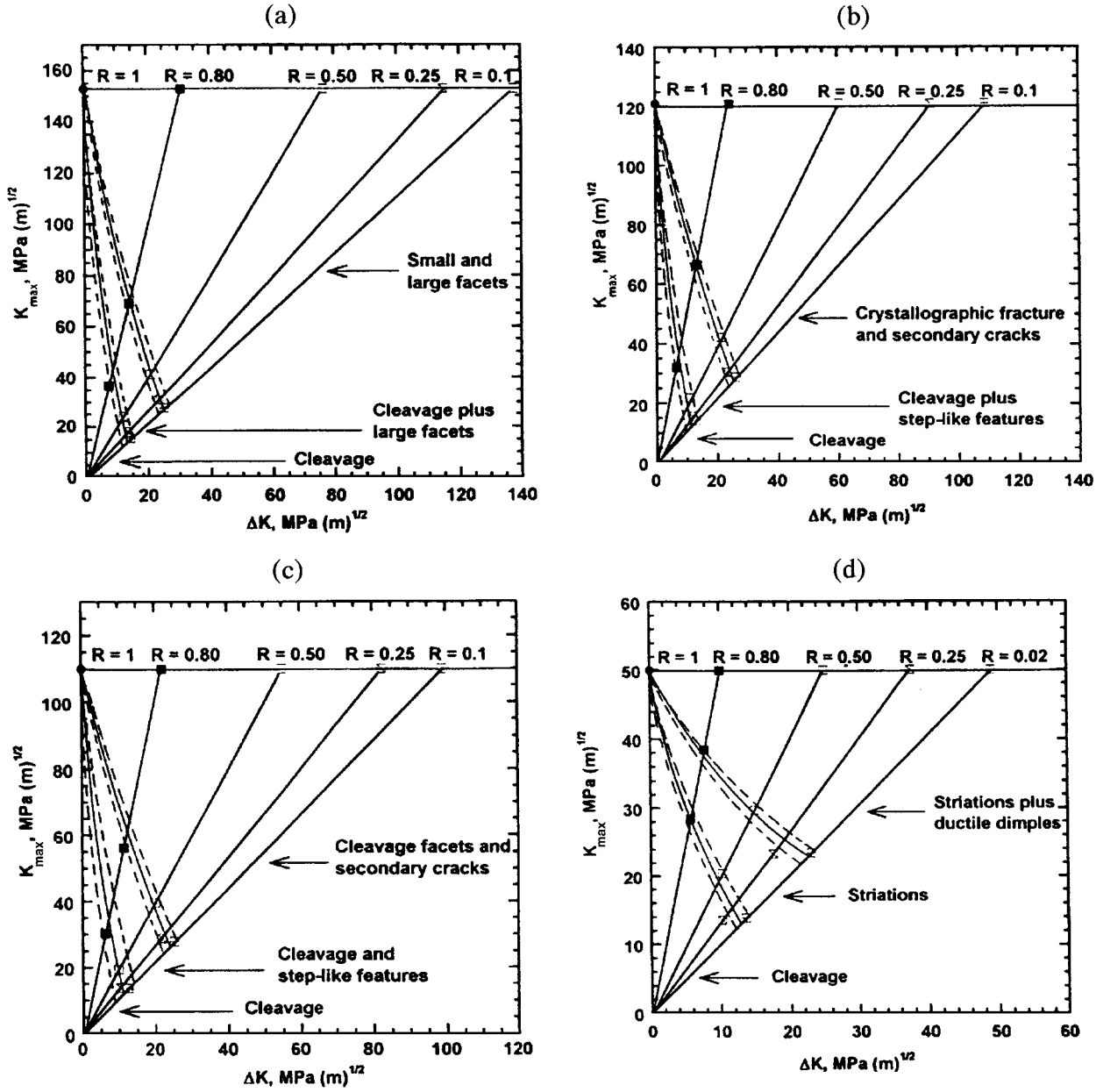

Figure 19 Fracture mechanism map showing the transitions between fatigue fracture modes in Ti-6Al-4V as a function of ΔK and K_{max}, for (a) microstructure A, (b) microstructure B, (c) microstructure C, and (d) microstructure D (continued on next page).

However, the fatigue crack growth rates in the mill annealed structure are generally faster in the Paris and high ΔK regimes (Fig. 7). Furthermore, the coarsest lamellar structure generally exhibits the slowest fatigue crack growth rates over the complete range of stress ratios and stress intensity factor ranges.

In the case of the colony material with the higher β volume fraction (microstructure A), the fatigue crack growth rates are comparable to those in the coarser colony microstructure B with a β volume fraction of $\sim$0.2 (Fig. 8). This is true over the complete range of stress ratios between 0.1 and 0.8. This suggests that increased β volume fraction is less effective than microstructural coarsening in the reduction of fatigue crack growth rates.

The slower fatigue crack growth rates in the coarser colony structures are associated with higher levels of crack deflection and roughness-induced crack closure in coarser microstructures. The shielding contributions from such microstructures have been modeled in a separate paper [32]. They will, therefore, not be considered further in this paper.

Instead, the rest of the discussion will focus on the two types of fracture maps that were obtained for Ti-6Al-4V (Fig. 19). The first type of map was obtained for the mill annealed microstructure (Fig. 19a). This has significant domains of flat, cleavage-like fracture modes in the near-threshold regime; striations in the Paris regime and striations and dimples in the high ΔK regime. In contrast, the second type of mechanism map was obtained for the colony microstructures (A–C). These maps are dominated by crystallographic 'step-like' fracture modes with large facets in the Paris regime, and smaller facets in the high ΔK regime (Fig. 19). Such maps may, therefore, be useful in the indentification of loading histories associated with the cyclic loading of Ti-6Al-4V with equiaxed or Widmanstatten/colony microstructures.

6. Conclusions

The micromechanisms of fatigue crack growth have been studied in selected structural gas turbine engine alloys (Inconel 718, single crystal PWA 1472 and Ti-6Al-4V). The following conclusions have been reached from a detailed study of the dependence of fatigue failure modes on ΔK and K_{max}:

1. The fatigue fracture modes in polycrystalline Inconel 718 and single crystal PWA1472 are crystallographic in nature up to mid-ΔK levels. In the Paris (steady state) regime, this transitions to a classical striation mechanism in the polycrystalline alloy and a cleavage-like mechanism with associated striations in the single crystal alloy. The faster fatigue crack growth rates in the high ΔK regime, particularly very close to final failure, is associated with a combination of fatigue and ductile-dimple (static) fracture modes. The incidence of ductile-dimple fracture also increases with increasing ΔK and K_{max} in this regime.

2. The fatigue fracture modes in Ti-6Al-4V depend strongly on the microstructural morphology. In the case of equi-axed α/β structures, a flat cleavage-like fracture mode is observed in the near-threshold regime. This transitions to a fatigue striation mode in the Paris regime. Finally, a combination of striations and ductile-dimples is observed in the high ΔK regime. However, in the case of lamellar α/β colony structures, faceted crystallographic fracture modes are observed in the near-threshold, Paris and high-ΔK regimes. The fracture surface roughness increases with increasing ΔK and K_{max}, and a combination of ductile-dimples and crystallographic fracture is observed in the high-ΔK regime. The incidence of ductile-dimple fracture also increases with increasing ΔK and K_{max}.

3. The fatigue fracture modes at positive stress ratios ($0 < R < 1$) can be summarized in fatigue mechanism maps that correspond to a triangular domain within a plot of K_{max} (ordinate) versus ΔK (absissa). Within such plots, the upper bound value of K_{max} corresponds to the fracture toughness, K_{Ic}. Also, the values of ΔK and K_{max} corresponding to constant R-ratio tests are characterized by straight lines that radiate outwards from the origin. The transitions from the near-threshold to the paris and high-ΔK regimes are characterized by curves that radiate outwards from the same point on the ordinate where $K_{max} = K_{Ic}$. Fatigue maps have been presented in this paper for Inconel 718, PWA 1472 and Ti-6Al-4V.

Acknowledgments

The results presented in this paper were obtained from programs supported by the Division of Materials Research of the National Science Foundation (NSF), the Federal Aviation Authority (FAA) and the Office of Naval Research (ONR). The authors are grateful to the Program Managers at NSF (Dr. Korukonda Murty and Dr. Bruce McDonald), FAA (Mr. Joe Wilson and Mr. Bruce Fenton) and ONR (Dr. George Yoder) for their encouragement and support.

References

1. J. M. ILSTON, J. M. DINWOODIE and A. A. SMITH, "Concrete, Timber and Metals" (Van Nostraand Reinhold, 1979).
2. "ASM Handbook on Fractography" (ASM International, Metals Park, OH, 1995).
3. D. HULL, "Fractography" (Cambridge University Press, 1999).
4. S. SURESH, "Fatigue of Materials," 2nd ed. (Cambridge University Press, 1999).
5. P. PARIS, M. P. GOMEZ and W. P. ANDERSON, *The Trend in Engineering* **13** (1961) 9.
6. A. K. VASUDEVAN and K. SADANANDA, *Metall. Trans.* **26A** (1995) 1221.
7. C. MERCER, A. B. O. SOBOYEJO and W. O. SOBOYEJO, *Acta Materialia* **47** (1999) 2727.
8. *Idem.*, *Materials Science and Engineering* A **270** (1999) 308.
9. S. SHADEMAN, A. B. O. SOBOYEJO, J. F. KNOTT and W. O. SOBOYEJO, *ibid.* A **315** (2001) 1.
10. S. DUBEY, A. B. O. SOBOYEJO and W. O. SOBOYEJO, *Acta Mater.* **45** (1997) 2777.
11. F. H. FROES, D. EYLON and H. B. BOMBERGER, "Titanium Technology: Present Status and Future Trends" (Titanium Development Association, 1985).
12. E. W. COLLINGS, "The Physical Metallurgy of Titanium Alloys" (American Society for Materials, Metals Park, OH, 1984).
13. I. J. POLMEAR, "Light Alloys: Metallurgy of the Light Metals," 3rd ed. (Halsted Press, 1996).
14. The Jet Engine, Rolls-Royce Plc., BPCC Ltd., 1986.
15. E. A. LORIA, (ed.) in Proceedings of the International Symposium on Superalloy 718: Metallurgy and Applications (TMS, Warrendale, PA, 1989).
16. Proceedings of the International Symposium on Superalloys 718, 625, 706 and Various Derivatives, E. A. Loria (ed.) (TMS, Warrendale, PA, 1997).
17. D. P. DELUCA and T. WATKINS, in Proceedings of the International Symposium on Superalloys 718, 625, 706 and Various Derivatives, edited by E. A. Loria (TMS, Warrendale, PA, 1997).
18. R. O. RITCHIE, *International Metals Reviews* **20** (1979) 205.
19. R. O. RITCHIE and J. F. KNOTT, *Acta Metall.* **21** (1973) 639.
20. V. SINHA, C. MERCER and W. O. SOBOYEJO, *Materials Science and Engineering* A **287** (2000) 30.
21. S. SHADEMAN and W. O. SOBOYEJO, *Materials Science and Engineering* in Press.
22. J. E. KING, *Fatigue of Engineering Materials and Structures* **5** (1982) 177.
23. B. A. LERCH and S. D. ANTOLOVICH, *Metall. Trans.* **21A** (1990) 2169.
24. M. B. HENDERSON and J. W. MARTIN, *Acta Metall.* **44** (1996) 111.
25. P. A. S. REED and J. E. KING, *Scripta Metall. Mater.* **26** (1992) 1829.
26. J. E. KING, *Materials Science and Technology* **3** (1987) 750.
27. U. GLATZEL and M. FELLER-KNIEPMEIER, *Scripta Metall. Mater.* **25** (1991) 1845.
28. D. J. MORRISON, V. CHOPRA and J. W. JONES, *ibid.* **25** (1991) 1299.
29. R. RAHOUADJ, J. MENIGAULT and M. CLAVEL, *Materials Science and Engineering* **93** (1987) 181.
30. S. CHEN and G. GOTTSTEIN, *J. Mater. Sci.* **24** (1989) 4094.
31. D. L. DAVIDSON and K. S. CHAN, *Acta Metall.* **37** (1989) 1089.
32. S. SHADEMAN, V. SINHA, A. B. O. SOBOYEJO and W. O. SOBOYEJO, *Mechanics and Materials*, submitted.
33. C. A. ZAPPFE and C. O. WORDEN, *Trans. ASM* **43** (1951) 958.
34. C. LAIRD and G. C. SMITH, *Phil. Mag.* **8** (1962) 847.

Received 5 December 2001
and accepted 3 July 2002